

# Spin-Wave Optics in YIG Realized by Ion-Beam Irradiation

Martina Kiechle, Adam Papp, Simon Mendisch, Valentin Ahrens, Matthias Golibrzuch, Gary H. Bernstein, Wolfgang Porod, Gyorgy Csaba, and Markus Becherer\*

Direct focused-ion-beam writing is presented as an enabling technology for realizing functional spin-wave devices of high complexity, and demonstrate its potential by optically-inspired designs. It is shown that ion-beam irradiation changes the characteristics of yttrium iron garnet films on a submicron scale in a highly controlled way, allowing one to engineer the magnonic index of refraction adapted to desired applications. This technique does not physically remove material, and allows rapid fabrication of high-quality architectures of modified magnetization in magnonic media with minimal edge damage (compared to more common removal techniques such as etching or milling). By experimentally showing magnonic versions of a number of optical devices (lenses, gratings, Fourier-domain processors) this technology is envisioned as the gateway to building magnonic computing devices that rival their optical counterparts in their complexity and computational power.

## 1. Introduction

A major motivation behind magnonics research is to replicate the functionality of bulky optical components in chip-scale devices that are amenable to integration with microelectronic circuitry.<sup>[1–7]</sup> This way, the functionality of coherent optical computers could also be cloned in the magnonic domain. Spin waves (SWs) display interference phenomena that resemble that of optical waves, but they offer submicron (possibly sub-100 nm) wavelength and can be launched and detected by electrical means. Chip-scale optically-inspired devices also provide a

pathway to much needed energy-efficient neuromorphic and edge-AI computing components.<sup>[8,9]</sup>

It has, however, remained elusive to produce spin-wave optics that approach the “ideal” behavior of optical components. This is largely due to the fact that so far no practical technology has been demonstrated to control the propagation characteristics of spin waves to the extent that is possible in optics. Ideally, one would want to realize any fine-grained spatial distribution of the index of refraction, as this provides a high degree of freedom in device design.

Magnonic devices are almost exclusively made from yttrium iron garnet (YIG) substrates, having low attenuation that en-

ables propagation over long distances. Lithographic patterning of YIG films allows defining some spin-wave optic functions<sup>[10]</sup> but has technological challenges,<sup>[11,12]</sup> as etched or milled film edges introduce undesired behaviors.<sup>[13]</sup> Even a well-controlled YIG patterning technology would be insufficient to replicate the propagation of electromagnetic waves, which propagate in vacuum, and optical devices can be made by patterning a transparent material to an appropriate shape. Essentially, refractive spin-wave optics need additional materials or intrinsic YIG film modifications, as magnons do not propagate in air.

A few pathways have been proposed to realize engineered YIG substrates. It is possible to use localized magnetic fields to steer spin waves,<sup>[14]</sup> but this requires a second magnetic layer to generate the fields and arbitrarily-shaped field profiles cannot be realized. Previous work has shown the use of heat distributions<sup>[15]</sup> to generate refraction-index profiles, a solution likely impractical in chip-scale devices. Local exchange bias may also be used for magnonic optics,<sup>[16]</sup> but so far this works only on metallic systems, which are highly-damping in nature.


In multilayered magnetic systems, it is well established that focused ion beam (FIB) irradiation modifies the magnetic properties<sup>[17,18]</sup> without actually removing material or creating edges. The FIB irradiation affects magnetic properties on a sub-50 nm size scale, which is a resolution that is hardly achievable by the combination of lithography and etching. The effect of FIB on magnetic multilayers motivated our work to study the effects of direct FIB-ing on the magnetic properties of YIG. Using 50 keV gallium ions ( $\text{Ga}^+$ ), the applied ion doses are chosen to not physically remove material, but to implant  $\text{Ga}^+$  into the YIG thin film and locally alter the crystalline structure.

In our work, we first demonstrate the effect of FIB irradiation on spin waves in YIG for plane-wave propagation and

M. Kiechle, S. Mendisch, V. Ahrens, M. Golibrzuch, M. Becherer  
School of Computation  
Information and Technology  
Technical University of Munich  
85748 Garching, Germany  
E-mail: markus.becherer@tum.de

A. Papp, G. Csaba  
Faculty of Information Technology and Bionics  
Pázmány Péter Catholic University  
Budapest 1083, Hungary

G. H. Bernstein, W. Porod  
Department of Electrical Engineering  
University of Notre Dame  
Notre Dame, IN 46556, USA

 The ORCID identification number(s) for the author(s) of this article can be found under <https://doi.org/10.1002/smll.202207293>.

© 2023 The Authors. Small published by Wiley-VCH GmbH. This is an open access article under the terms of the Creative Commons Attribution License, which permits use, distribution and reproduction in any medium, provided the original work is properly cited.

DOI: 10.1002/smll.202207293

characterize the dependence of magnonic wavelength on FIB dose, obtaining an index of refraction  $n$ . Lenses and diffraction gratings are designed with a binary irradiation pattern—in a similar fashion to elementary optical devices, where light propagates either through glass or vacuum.

We find that the effect of FIB irradiation on YIG films can be modeled adequately by assuming an effective magnetization value  $M_{\text{eff}}$  that varies with the FIB dose, which is in agreement with the findings in another work.<sup>[19]</sup> The locally changed  $M_{\text{eff}}$  results in a local change of the wavelength, which, in turn, may be modeled as a spatially varying index of refraction  $n$ . As a consequence, FIB irradiation allows the realization of (almost) arbitrary 2D  $n$  profiles.

Going beyond binary patterns, we demonstrate that FIB irradiation is especially useful for graded-index (GRIN) magnonics<sup>[20,21]</sup> as it allows a continuous and high-resolution variation of  $n$  across the film surface. As a highly meaningful example of such systems, a 4f Fourier-domain signal processor is shown in Section 3. The demonstration of a 4f system opens the door to the realization of a variety of optically-inspired computing systems<sup>[22]</sup> using magnons. We envision that the FIB technology shown here will readily provide access to magnonic devices that may rival on-chip optics in their functionality, and consequently act as the gateway to magnonic integrated circuits (in analogy to photonic ICs). While spin waves have limitations, such as damping that should be compensated by some amplification mechanism for large-scale devices, they have benefits, such as nonlinearities,<sup>[9,23]</sup> that open up applications unreachable for photonic ICs.

## 2. Experimental Section

The effect of FIB irradiation was characterized by recording the SW waveform using longitudinal time-resolved magneto-optical Kerr effect microscopy (trMOKE) and determining the SW wavelength change at various ion-dose levels. **Figure 1** gives an overview of the experimental techniques used for fabrication

and metrology. An in-house sputter-deposited YIG thin film (thickness  $t = 100$  nm) with co-planar microwave antennas (signal, gap width  $S$ ,  $G = 2\text{--}5$   $\mu\text{m}$ ) was bonded to a PCB board from where it was fed with a microwave signal. Areas next to the excitation antennas were FIB-irradiated at different ion doses and shapes. Fabrication details can be found in Section S5, Supporting Information. Subsequently, 2D spin-wave patterns were imaged with a longitudinal, time-resolved Kerr microscope in forward volume configuration. The scale bar in all these images represented the Kerr signal of the trMOKE microscope, and were scaled in arbitrary units. The signal amplitude was not calibrated, so these values cannot necessarily be directly compared.

In the custom-built trMOKE apparatus (for details, see Section S5, Supporting Information) the film was magnetized out-of-plane (along  $M_z$ ) and the dynamic  $m_x$  and  $m_y$  components display wave propagation. The FVSW mode was isotropic and therefore showed the closest analogy to optical wave propagation. The spatial resolution of the trMOKE was limited to  $\approx 0.4$   $\mu\text{m}$  due to the smallest possible step size of the  $x$ - $y$  stage, as well as the optical diffraction limit of the applied laser lightsource and the objective lens, limiting the shortest detectable spin-wave wavelength to about  $\lambda = 1$   $\mu\text{m}$ . The FIB pixel size (beam diameter + dwell space) can be as small as 10 nm, meaning the writing technique can be applied to small-scale geometrical shapes way beyond the optical detection limit.

### 2.1. Characterizing the Effect of FIB Irradiation in YIG

50 keV accelerated gallium ions ( $\text{Ga}^+$ ) were used to irradiate YIG thin films at ion doses ranging from  $1 \times 10^{12}$  to  $1 \times 10^{15}$  ions  $\text{cm}^{-2}$ , with the purpose of manipulating the magnetic properties locally. As a dose calibration method, regions with linearly increasing ion doses were irradiated next to the excitation antenna and the SW wavelength changed due to a modification of the effective magnetization  $M_{\text{eff}}$  was measured.

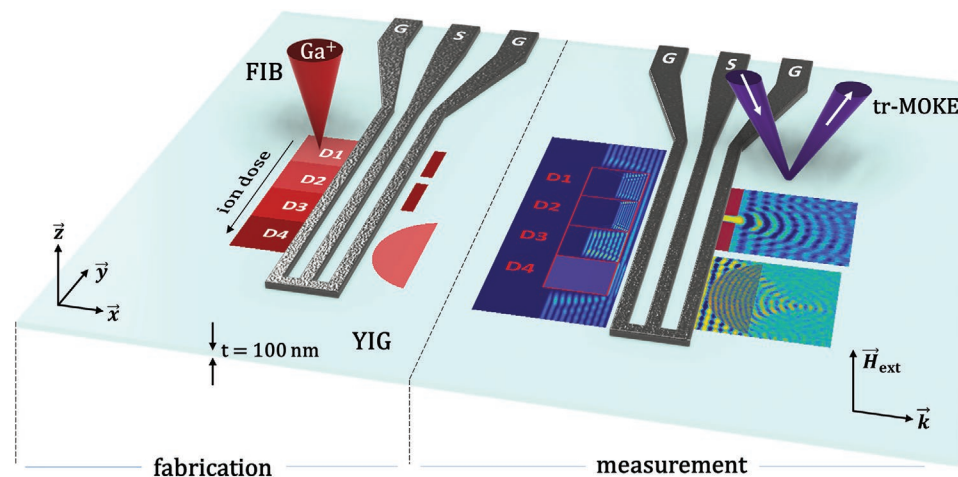


**Figure 1.** Representation of the experimental arrangement. Left part: areas in YIG next to the excitation antenna are directly irradiated with FIB at different ion-dose levels (indicated by the intensity of the red color), and an ion-dose dependent change of  $M_{\text{eff}}$  is found. This is used for the application examples: a lens at a low dose with a modified  $n$  and a single slit at a high dose. Right part: spin-wave propagation patterns in the FIB-irradiated regions are imaged with trMOKE.

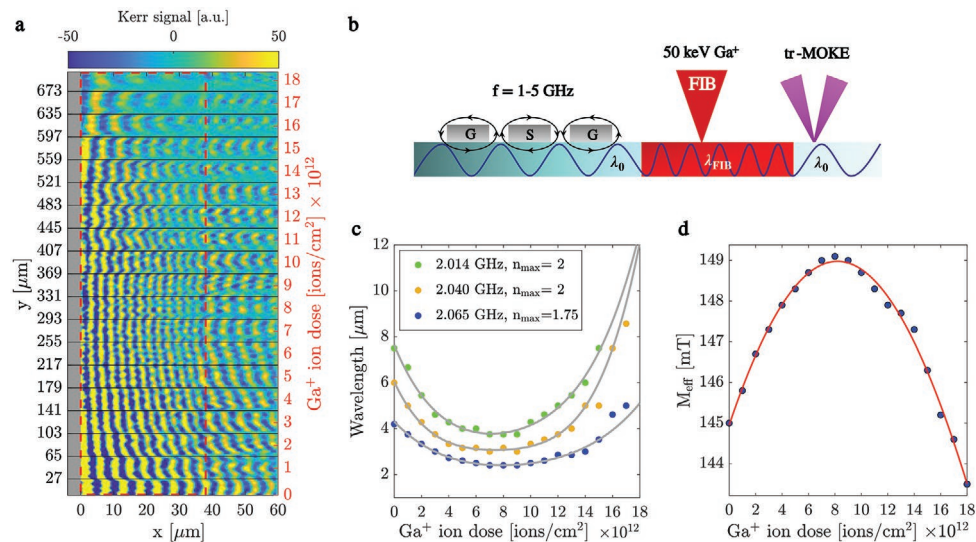


**Figure 2.** Illustration of the ion dose dependent change of  $M_{\text{eff}}$  in YIG. a) trMOKE image of coherently excited spin waves (groundline of antenna shown on the left) in regions of linearly increasing ion doses (separated by horizontal lines, irradiated area indicated by red frame). The bottom row shows the actually excited wavelength in unirradiated YIG. b) 1D sketch of the experiment: The area next to the excitation antenna is FIB irradiated, whereby the magnetization and hence the wavelength is locally changed. c) Wavelength change versus ion dose profile at different frequency settings with an external field of 214 mT. d) Ion-dose-dependent change of  $M_{\text{eff}}$ , numerically calculated from the SW dispersion relation.

**Figure 2** shows the resulting wavelength profiles versus the applied ion dose.

The degree of change in the magnetic properties was dependent on the applied  $\text{Ga}^+$  ion dose and also on the acceleration voltage if the film thickness was larger than the ion penetration depth. The SRIM<sup>[24]</sup> simulated mean ion implantation depth of  $\text{Ga}^+$  in a 100 nm thick YIG film was 24 nm and makes about a third of the total thickness (considering the effective thickness due to, for example, Ga diffusion into the first few (atomic) layers, sputter-process imposed film thickness variations, etc.). Nonetheless, it was characterized how spin-wave propagation was affected in the effective layer and therefore the effect was modeled across the entire film thickness. Insights into FIB-irradiation-induced changes of YIG on the crystal level can be found in Section 5. As a main message, the reason is believed that the parameter changing the SW dispersion relation locally is  $M_{\text{eff}}$  was because a change in the resonance field on fully irradiated films was observed, which was solely dependent on  $M_{\text{eff}}$  and the applied frequency according to Kittel's equation. Furthermore,  $M_{\text{eff}}$  incorporated an anisotropy term that was likely to be affected by the FIB-induced strain in the crystal and potentially the underlying cause of the modification.

Interpreting the results in terms of micromagnetic parameters, it was found that FIB irradiation of YIG can be accurately modeled in terms of modifying  $M_{\text{eff}}$  and the magnetic damping  $\alpha$  ion-dose dependent. A low ion dose (up to  $6 \times 10^{12}$  ions  $\text{cm}^{-2}$ ) increased  $M_{\text{eff}}$ , and hence decreased the wavelength, while  $\alpha$  increased only moderately (see Figure 2c,d). For higher ion doses, a turning point was reached and  $M_{\text{eff}}$  decreased again until spin-wave propagation was inhibited (doses larger than  $1 \times 10^{14}$  ions  $\text{cm}^{-2}$ ). There were multiple reasons why spin waves were not seen at higher doses. First, as the wavelength went up, the excitation efficiency of the coplanar waveguide

diminishes. At even higher doses the cutoff frequency for spin waves (ferromagnetic resonance frequency) increased above the excitation frequency, thus spin waves were completely inhibited. Measuring these regions at higher frequencies was possible, and the damping was still not critically high. The wavelength versus ion dose profile was non-linear and frequency-dependent due to the inherent non-linear dispersion relation of spin waves. In the low-dose regime,  $M_{\text{eff}}$  was slightly increased, which was used for the demonstration of optical elements with a distinct refractive index in analogy to glass.

Applications of higher complexity, such as continuous refractive media, can be modeled by saturation-magnetization landscapes. Using FIB, this meant changing the ion dose point by point. Alternatively, it was also possible to change the filling factor in pixel space to set the value of  $M_{\text{eff}}$ . This way, only a single ion dose had to be applied, and the average magnetization was changed due to a density gradient. A pixel size of 40 nm was used in the experiments (can go as low as 10 nm), which was about two orders of magnitude smaller than the applied spin-wave wavelength. This technique (demonstrated in Section 3.2) was well suited for continuously changing wave propagation properties, as was done with GRIN optics.<sup>[21]</sup>

A more trivial (but often-needed) use of FIB irradiation was to apply a high dose that entirely blocks propagation, or, in other words, destroyed the magnetic properties ( $M_{\text{eff}} = 0$ ), and hence reflected SWs, such as shown in ref. [25]. This allowed the creation of refractive and diffractive optics using the same tools.

## 2.2. Tuning the Magnonic Index of Refraction and Saturation Magnetization by FIB

In order to design spin-wave “replicas” of optical devices, it was instructive to define the magnonic index of refraction  $n$ .

The effective change of the magnonic refractive index  $n_{\text{eff}}$  was extracted from the wavelength change in the untreated versus the irradiated YIG film part ( $\lambda_0$  vs  $\lambda_{\text{FIB}}$ )

$$n_{\text{eff}} = \lambda_0 / \lambda_{\text{FIB}} \quad (1)$$

The highest achievable refractive index  $n_{\text{max}} = \lambda_0 / \lambda_{\text{min}}$  corresponded to the ion dose that generated the highest  $M_{\text{eff}}$ , and hence the smallest possible wavelength  $\lambda_{\text{min}}$  with respect to the initial parameters. In order to model the correlation of FIB irradiation and the magnetic properties, the effect of FIB was best understood as an ion-dose dependent change of the effective magnetization  $\Delta M_{\text{eff}} = M_{\text{eff,FIB}} - M_{\text{eff,0}}$ . The results are shown in Figure 2d (see previous section for details). Due to the highly nonlinear nature of the magnonic dispersion relation,  $n_{\text{eff}}$  was only valid for a certain spin-wave frequency  $f$  and the corresponding wavelength  $\lambda_0$ . Wavelengths  $\lambda_0$  that can be efficiently excited and detected by the coplanar waveguide antennas in use were targeted. Generally, the refractive index for a specific wavelength can be calculated by numerically solving the SW dispersion relation<sup>[26]</sup> for  $k$ -vectors at the initial  $M_{\text{eff,0}}$  and for  $M_{\text{eff,FIB}}$  at the respectively chosen ion dose

$$n_{\text{eff}} = k(M_{\text{eff,FIB}}, f, H_{\text{ext}}, t, A_{\text{exch}}) / k(M_{\text{eff,0}}, f, H_{\text{ext}}, t, A_{\text{exch}}) \quad (2)$$

In Equation (2),  $f$  is the microwave frequency used for excitation,  $H_{\text{ext}}$  the applied bias field normal to the film plane (forward volume),  $t$  is the film thickness, and  $A_{\text{exch}}$  is the exchange stiffness. This approach of defining a refractive index profile was similar to previous works, where a micromagnetic modeling of the dispersion relation was used for spin-wave lenses with a thickness or magnetization gradient.<sup>[27,28]</sup>

## 3. Results

### 3.1. Design and Fabrication of Optically Inspired Magnonic Elements

To replicate the behavior of conventional optical elements (i.e., glass lens), one may utilize a single modified refractive index  $n_{\text{eff}}$  value in addition to that of intrinsic YIG (where  $n_{\text{eff}} = 1$ ). Figure 3a shows a trMOKE image of a plano-convex lens realized with this binary technique.

The Lensmaker's equation<sup>[29]</sup> is used for the given refractive index of 1.8 at a dose of  $7 \cdot 10^{12}$  ions  $\text{cm}^{-2}$ . This is the maximum  $n_{\text{eff}}$  change achievable at this wavelength. The lens has a curvature radius of 30  $\mu\text{m}$  and thickness of 20  $\mu\text{m}$ , resulting in a focal distance of about 37  $\mu\text{m}$ . The trMOKE measured image of the lens reveals parameters closely matching the design target calculated from the optical formulas. The focal amplitude is weak compared to the excitation, probably because reflections occur on the surfaces of the lens and damping is slightly higher in this particular sample, but the focusing is clearly visible nonetheless. A different way of using the FIB irradiation is shown in Figure 3c, where we show single-slit spin-wave diffraction achieved by locally destroying the magnetization in the red areas through irradiation at a high ion dose of  $1 \times 10^{15}$  ions  $\text{cm}^{-2}$ . The resulting diffraction pattern is a mixture of the expected diffraction pattern for a single slit, and a plane wave that couples through from behind the FIB irradiated part. To complete the parallels with elementary optical components, Figure 3b demonstrates a circular-shaped source focusing spin waves at a distance that equals the radius. The curved surface acts as a secondary spin-wave source, where spin precession is driven by the high-amplitude, spatially-uniform oscillations of the area between its spherical backside and the excitation antenna. The primary non-linear precession excites linear spin waves on the inside of the circle via dipole coupling, a mechanism explored in ref. [25].

Another useful focusing instrument in optics is the zone plate, where the focal distance is a function of lateral geometry, particularly the arrangement of the zones as opposed to thickness and curvature, as it is the case for conventional lenses. In the following, we use the properties of a Fresnel zone plate to demonstrate three different working mechanisms depending on distinct operation regimes of the FIB irradiation with respect to ion dose. In the first case, we use a low ion dose to create a phase shift, in the second case, a high-dose irradiation locally blocks SW propagation, and in the third case, SW transmission is completely inhibited with a high-dose region, and spin waves are excited indirectly on the patterned edge via dipole coupling.

A key function in optics is the ability to shift the phase of waves, and we show this feature by the example of a Fresnel phase plate in Figure 4a.

The focusing effect occurs via constructive interference of beams propagating with respect to a  $180^\circ$  phase difference to each other. This phase shift is achieved by the change of  $n$  over the 6  $\mu\text{m}$  length of the zones (semi-transparent red overlays)

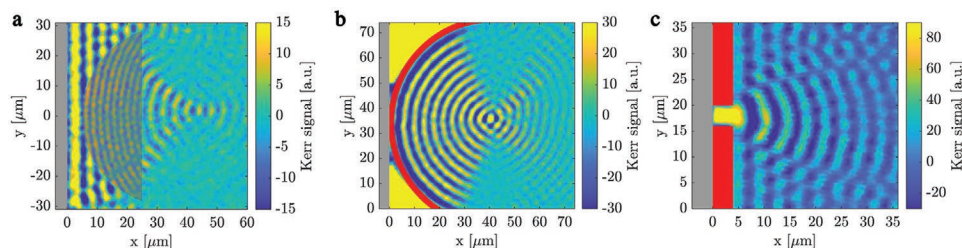


**Figure 3.** Demonstration of refractive, diffractive and reflective optical components fabricated with FIB irradiation, recorded with trMOKE. a) D-shaped spherical lens with a curvature radius of 30  $\mu\text{m}$  and a clearly shortened wavelength in the inside (semi-transparent red,  $n \approx 1.8$ ). b) A semicircular source ( $R = 40 \mu\text{m}$ ) with spin waves excited through the high-amplitude resonance behind the circle. The high-amplitude region appears as a saturated yellow region. Red lines indicate a high FIB dose that blocks spin wave propagation. c) An “optical” slit (4  $\mu\text{m}$  width).



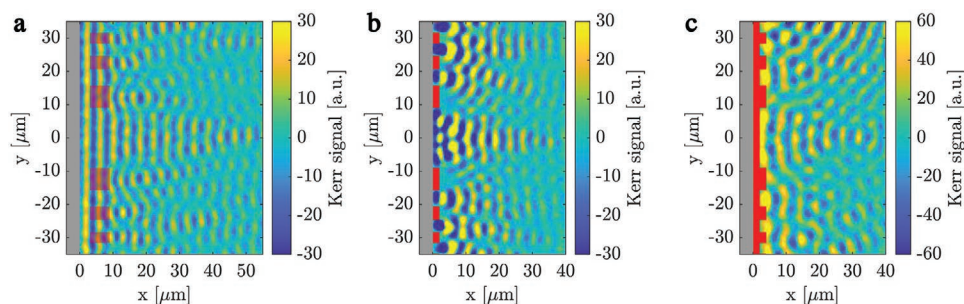


**Figure 4.** Spin-wave diffraction and focusing in FIB-treated regions (red areas) by reference to an optical (Fresnel) zone plate, visualized with trMOKE. Different ion doses are used for distinct operating mechanisms. a) Phase-shift-induced focusing achieved with a low ion dose. The shortened wavelength in the FIB areas exits the zones with a phase shift close to  $180^\circ$ . b) A high ion dose that causes a local barrier for spin waves, analogously to an optically opaque region. c) A blocking wall before the actual zone plate in combination with a high excitation amplitude excites spin waves via dipole-field coupling on the back surface. The low and high parts of the zone plate create an initial relative phase difference necessary for focusing.

so that the  $180^\circ$  phase difference occurs at the zone plate's exit plane from the difference of the wavelengths. Here, an ion dose of  $7 \times 10^{12}$  ions  $\text{cm}^{-2}$  was used, as it creates the largest difference in  $n$ , and the length was chosen with the help of a supplementary experiment (Figure S1b, Supporting Information). Alternatively to this phase-shift-based zone plate, a Fresnel zone plate can be realized by simply blocking waves in the regions where they would destructively interfere at the desired focal point. In this device (Figure 4b) the phase shifters are replaced by regions fabricated with a large ion dose (red lines irradiated at a dose of  $1 \times 10^{15}$  ions  $\text{cm}^{-2}$ ). A third zone-plate demonstration uses the effect we also exploited in the circularly shaped source in Figure 3b, that is, a coherent wavefront is created at the boundary of a high-dose region. By shifting the wavefront about  $\lambda/2$  between the zones, the desired focusing effect is achieved, as shown in Figure 4c). The geometrical arrangement of the zones is chosen to focus a  $4 \mu\text{m}$  wavelength at a distance of  $40 \mu\text{m}$  from the exit plane. Since the excited wavelength is different in (a–c), the observed focal distance varies accordingly. Diffractive devices demonstrate the high resolution of FIB patterning and serve as proof that negligible damage is caused outside the irradiated area in the YIG films.

### 3.2. Gradient-Index and Fourier Optics for Spin Waves

In Fourier optics,<sup>[30,31]</sup> linear processing functions mostly rely on the Fourier-transform property of lenses—easily moving between the real and the Fourier domain enables a number of signal processing primitives. Similarly, Fourier-optics devices for spin waves could serve as building blocks for useful computing and information-processing functions.

Perhaps the most illustrative of Fourier optics devices is the  $4f$  system illustrated in Figure 5a. The image (encoded in wave amplitude and phase on the image plane) is Fourier transformed by the first lens and this Fourier transform appears in the Fourier plane, which is inverse-Fourier transformed by the second lens. Any Fourier-domain manipulation of the image (such as filtering, convolution, matched filtering) can be accomplished by a filter placed in the Fourier plane that alters the magnitude and/or phase of the spectral components of the image.

While Fourier optics components could be put together from concave lenses such as the one shown in Figure 3a, the lens boundaries introduce undesired reflections and diffraction effects, which can largely be avoided in graded-index (GRIN) optics, where the wave steering is done with a gradually changing refractive index across the fiber diameter instead of introducing geometrical modifications with a singular index. Consequently, graded-index magnonic elements require the ability to realize gradually changing magnetic properties, such as simulated in ref. [7]. Since FIB irradiation can continuously tune  $n_{\text{eff}}$  of a magnetic film by changing the filling factor of an image in pixel space, we can create a magnetization landscape of arbitrary shape, including a GRIN lens<sup>[15]</sup> or GRIN fibers.<sup>[32]</sup> Graphically, FIB-ing an image with every other pixel irradiated is the equivalent of half the ion dose, and the amplitude of a desired profile can be used to determine the filling ratio locally. Since the pixel size is much smaller than the SW wavelength, spin waves experience a smooth transition.

To produce a refractive-index gradient of a certain shape, the ion-dose profile needs to be determined for the desired wavelength (or index of refraction) profile. Here we used the measurements from Figure 2c. In case of a GRIN lens, the wavelength profile for a parabolic refractive-index change can be written as<sup>[33]</sup>

$$\lambda = \frac{\lambda_{\text{FIB}}}{1 - 0.5(2\pi\gamma/4f)^2} \quad (3)$$

Hereby,  $\lambda_{\text{FIB}}$  is the resulting wavelength of the ion dose used for the design (ideally the smallest achievable wavelength),  $\gamma$  is the lateral distance from the optical axis, and  $f$  is the desired focal length of the lens. For the calculation of the required ion-dose profile that results in the desired magnetization gradient, we used the ion dose versus wavelength profile from Figure 2c and inserted the inverted version into the GRIN lens wavelength profile [Equation (3)], resulting in the ion-dose profile in Figure 5b. This profile is used for the density distribution of the FIB image in pixel space, and the 2D irradiation pattern of a  $4f$  GRIN lens with a diameter of  $18.5 \mu\text{m}$  and a length of  $76 \mu\text{m}$  is shown in Figure 5c. Experimentally, this image is irradiated at a peak ion dose of  $5.2 \times 10^{12}$  ions  $\text{cm}^{-2}$ , resulting in respectively lower doses across the diameter due to the density variation.

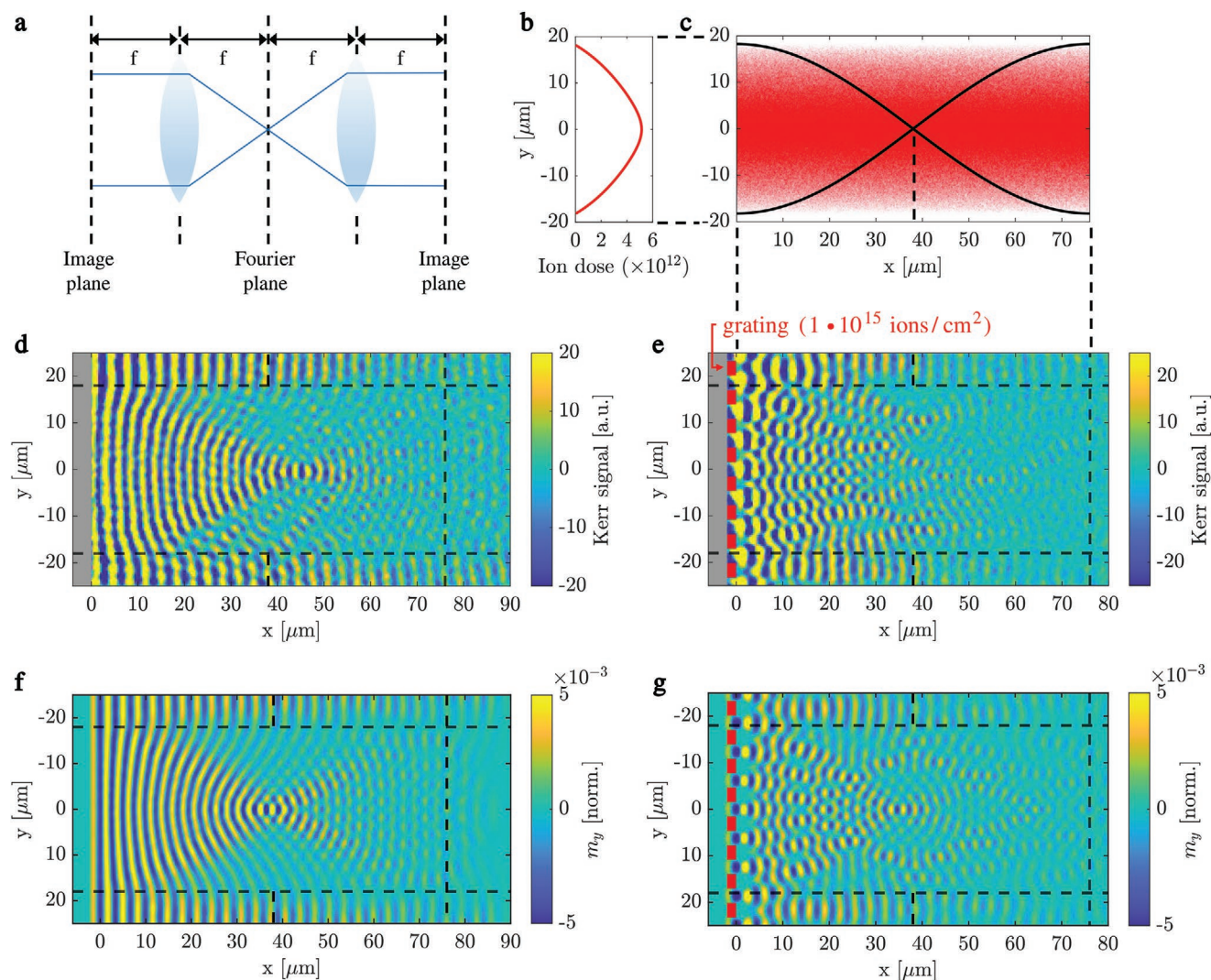


**Figure 5.** Demonstration of a 4f system for spin waves realized with a FIB-irradiated graded-index magnetization. a) Working principle of a conventional 4f system based on two consecutive lenses. b) 1D ion-dose profile calculated from the measured wavelength change versus ion dose profile. c) 2D irradiation pattern (binary) of a full pitch GRIN lens realized by a filling-factor variation in the FIB image. d) trMOKE image of the GRIN lens irradiated in YIG. e) A diffraction grating is irradiated at the anterior plane. The system images the first order diffraction at  $30^\circ$  on the Fourier plane. f, g) show the corresponding simulations for (d) and (e), performed with the calculated magnetization gradient and expected damping, respectively.

Note that the image in Figure 5c is binary, that is, only one global ion dose (red) is used for the irradiation.

The measured spin-wave profile of the fabricated GRIN lens—performing a Fourier transform of the plane wave excited by the microwave antenna right behind the lens—is shown in Figure 5d. (To avoid confusion, we note here that this is a full-pitch GRIN lens, thus the Fourier plane and the second image plane fall both inside the lens.) The focal distance is slightly longer than the design value ( $45\ \mu\text{m}$  instead of  $38\ \mu\text{m}$ ), which is most likely a result of a bias field inaccuracy or a deviation from the desired ion dose. At the exit plane, a reverse FT should occur, that is, the plane wave is reconstructed. Due to the slightly longer focal length, the experimental lens is less than a full pitch, thus the waves at the exit are still slightly divergent.

To demonstrate FT properties of this GRIN lens, we irradiated a diffraction grating in front of the GRIN lens entrance plane by using a high dose, as shown in the slit experiment in

Figure 3b. The grating is designed to have a diffraction angle of  $30^\circ$  for  $\lambda_0 = 3.1\ \mu\text{m}$  wavelength (grating constant  $= 2\lambda_0 = 6.2\ \mu\text{m}$ , thickness  $= 2\ \mu\text{m}$ ). The expected Fourier plane (FP) should occur at  $38\ \mu\text{m}$ , and we observe a slight deviation that has also occurred in the focal distance when we tested the GRIN lens with a plane wave. The occurring focal points left and right of the center peak in the FP represent the first-order diffraction of the grating, and correspond to the expected diffraction angle. The inverse Fourier transform (image of the grating) at the exit plane at  $76\ \mu\text{m}$  is, however, too weak to be visible in the measurement, potentially because of too high damping.

We performed micromagnetic simulations using mumax<sup>3</sup> to provide a reference for the ideal GRIN-lens operation. We used the same geometry as in the experiment, with the same excitation frequency applied. The saturation magnetization of the YIG film ( $M_s = 121\ \text{kA m}^{-1}$ ) was determined using ferromagnetic resonance (FMR) measurements. The external bias field

( $B_{\text{ext}} = 221.8$  mT) was selected to match the experimental wavelength. In the irradiated regions, we used  $M_{\text{FIB}}^{\text{FIB}} = 122.85$  kA m<sup>-1</sup>, also selected to produce the same wavelength as in the irradiated regions in the experiments. This corresponds to a 1.5% change in saturation magnetization due to irradiation. We selected damping values to match the experimental decay,  $\alpha = 6 \times 10^{-4}$  and  $\alpha_{\text{FIB}} = 12 \times 10^{-4}$ , corresponding to a doubling in damping due to irradiation. Lateral discretization was set to 40 nm, with a single layer in the thickness direction (100 nm). The simulations closely match the experimental results, except for the focal length, which was equal to the design value in the simulations. The simulations show that the performance of our GRIN lens is mainly limited by two factors: 1) The relatively large damping in our films should be improved for a clear demonstration of recollimation/inverse Fourier transform. 2) Waves enter the GRIN lens from the sides due to diffraction, and these distort the interference patterns. For an improved demonstration, one should either limit the excitation of waves to the GRIN-lens input aperture, or block waves from entering through the sides. We suggest that this could be also realized using the proposed FIB technique.

#### 4. Discussion

We can group the presented devices based on multiple properties: First, some part of the devices in this paper are refractive, that is, ion irradiation is used for changing the effective refractive index in the specified region, while others are reflective or diffractive, that is, relatively high doses are used to produce a perimeter around the device geometry. Here, the saturation magnetization in the YIG film changes abruptly—practically falling to zero. In the former case, spin waves propagate through the irradiated region (although with modified dispersion), while in the latter case spin waves are blocked, reflected, or generated on the boundaries between the intrinsic and irradiated YIG regions. This brings us to the next distinction based on whether the device is used for manipulating an incident wavefront or if it is used to indirectly excite a wavefront with a desired shape. From the perspective of functionality, we have demonstrated elements for focusing waves and also diffraction gratings (the zone plates being a combination of the two). The most sophisticated demonstration we present here is the GRIN lens and the 4f system based on it, which contains a pointwise varying refractive irradiation that is used for focusing waves, combined with a diffraction grating that block parts of the incident wavefront in a periodic manner, transmitting only a single spatial-frequency component. The above distinctions provide justification of the rich selection of demonstrations in this paper, representing the flexibility and wide applicability of a single fabrication technique to implement a wide range of optical elements. This set of devices can be considered complete in the sense that a full linear signal processor might be realized based on them, as demonstrated through the 4f system.

The refractive-index modification for spin waves in YIG through a FIB-induced magnetization change can be accurately calculated from the ion-dose-dependent wavelength change. With this, we are able to design devices not only

where binary refractive arrangements are needed, but also create smooth magnetization transitions (gradients) that are essential in GRIN optics. With the strategy to use a half-toning technique (stochastic filling factor in pixel space) on the FIB image to produce an ion-dose gradient, one global ion dose can be used for the entire image, eliminating the need for multiple irradiation steps. Since the spotsizes of the FIB is two orders of magnitude smaller than the spin-wave wavelength, this simplification is not expected to degrade the device performance.

As the complexity of the 4f system is the highest among the presented devices, the limitations of the technology (spin waves and also our facilities) is the most evident here. It is visible in Figure 5d,e that damping limits the useful length of the GRIN lens to tens of wavelengths. We presume that our demonstration is not optimal from this perspective in multiple ways: with better-quality (homogeneity and damping) YIG films, and by optimization of parameters to achieve higher group velocity, we expect that it is possible to increase the propagation distance and thus the practical device size by at least an order of magnitude. There is also a limitation of the numerical aperture in the 4f system, which is posed by the limited variability of the effective saturation magnetization (and therefore the maximum achievable refractive index) induced by irradiation. Although we demonstrated that a refractive index comparable to optics is achievable ( $n \approx 1.8$ ), a higher change would improve the applicability and performance of magnonic devices. We see a potential improvement here, as we estimate that less than a third of the YIG film is affected by the FIB due to the shallow penetration depth. By using lighter ions, for example, He<sup>+</sup>, we expect that a stronger effect is achievable. Finally, a strong disturbance of the interference pattern is caused by the waves that are generated adjacent to the fabricated devices. This could be avoided by separating the device laterally from the neighboring structures, for which FIB irradiation could also be used, both for creating reflective and absorbing boundary conditions, exploiting the steeply increasing damping at moderately high doses.

Magnonic systems themselves have limitations, perhaps the most important one is the finite damping that limits the realizable device size and complexity. Thus, spin waves are not an ideal fit to directly replicate classical optical building blocks, instead, they are more suitable for the approaches used in nanophotonics<sup>[9,34]</sup>—we believe that our technique is also applicable to the realization of such structures, as the achievable resolution with FIB ( $\approx 10$  nm) can easily serve that. The automatic design of magnonic devices combined with a flexible and versatile fabrication method has the potential to raise the bar for magnonic device concepts, enabling the realization of circuits,<sup>[35]</sup> and drive the field toward practical applications.

In terms of applications, the 4f system (and similar constructions) carries the biggest potential. Based on the 4f system it is possible to realize a wide class of linear (Fourier domain) signal processing applications as it was well established in the field of optical computing.<sup>[31]</sup> Thus, successful implementation of 4f systems with spin waves may allow any linear signal-processing task to be implemented in the magnonic domain. Such tasks are essential building blocks of neuromorphic computing pipelines and are in great demand for edge AI tasks.<sup>[36]</sup>



## 5. Conclusion

Our paper presents FIB irradiation of YIG as a straightforward technology to manipulate the index of refraction precisely and in a quasi-continuous way, enabling chip-scale magnonic clones of optical components. We demonstrated various use cases how elements known from optics can be adapted in the spin-wave domain by using FIB. The FIB direct-writing technology offers flexible, rapid, high-resolution prototyping, while it avoids many challenges of traditional patterning methods, such as the inability to produce gradients and inevitably introducing defects on patterned edges. Although FIB itself is not directly applicable for mass production, the presented devices could be straightforwardly mass-produced using the implanter technology omnipresent in industrial settings.

Due to its flexibility, high resolution, wide availability and a path toward mass production, we believe that the presented technology has the potential to drive a magnonic revolution and turn spin-wave-based, chip-scale computing devices to a practical reality.

## Supporting Information

Supporting Information is available from the Wiley Online Library or from the author.

## Acknowledgements

The authors want to thank all staff members and researchers working in the lab facilities of ZEIT<sup>lab</sup>, and Tatyana Orlova and Maksym Zhukovski at the Imaging Facility at University of Notre Dame. The authors would also like to thank the motivated students involved in this project, especially Carolin Calcagno. Funding from the German Research Foundation (DFG No. 429656450), the German Academic Exchange Service (DAAD, No. 57562081) and the Bavaria California Technology Center (BaCaTeC) is acknowledged. A.P. received funding from the PPD research program of the Hungarian Academy of Sciences. G.C. acknowledges financial support from the Horizon 2020 Framework Program of the European Commission under FET-Open grant agreement no. 899646 (k-NET).

Open access funding enabled and organized by Projekt DEAL.

## Conflict of Interest

The authors declare no conflict of interest.

## Author Contributions

M.K., A.P., and M.B. conceived the ideas and conducted the experiments. A.P. designed and built the trMOKE microscope and advised in the measurements. M.K., A.P., G.C., and M.B. wrote the manuscript. All authors analyzed the results and reviewed the manuscript.

## Data Availability Statement

The data that support the findings of this study are available from the corresponding author upon reasonable request.

## Keywords

focused ion beam in yttrium iron garnet, optomagnonics, spin wave computing

Received: November 23, 2022

Revised: January 13, 2023

Published online: February 21, 2023

- [1] F. Groß, M. Zelent, N. Träger, J. Förster, U. T. Sanli, R. Sauter, M. Decker, C. H. Back, M. Weigand, K. Keskinbora, G. Schütz, M. Krawczyk, J. Gräfe, *ACS Nano* **2020**, *14*, 17184.
- [2] H. Dai, A. Xiao, D. Wang, Y. Xue, M. Gao, X. Zhang, C. Liu, Q. Lu, *J. Magn. Magn. Mater.* **2020**, *505*, 166756.
- [3] G. Csaba, Á. Papp, W. Porod, *Phys. Lett. A* **2017**, *381*, 1471.
- [4] H. Qin, R. B. Holländer, L. Flajšman, F. Hermann, R. Dreyer, G. Woltersdorf, S. van Dijken, *Nat. Commun.* **2021**, *12*, 2293.
- [5] H. Yu, G. Duerr, R. Huber, M. Bahr, T. Schwarze, F. Brandl, D. Grundler, *Nat. Commun.* **2013**, *4*, 2702.
- [6] G. Csaba, A. Papp, W. Porod, *J. Appl. Phys.* **2014**, *115*, 17C741.
- [7] C. S. Davies, V. Kruglyak, *Low Temp. Phys.* **2015**, *41*, 760.
- [8] Q. Wang, A. V. Chumak, P. Pirro, *Nat. Commun.* **2021**, *12*, 2636.
- [9] Á. Papp, W. Porod, G. Csaba, *Nat. Commun.* **2021**, *12*, 6422.
- [10] Á. Papp, W. Porod, Á. I. Csurgay, G. Csaba, *Sci. Rep.* **2017**, *7*, 9245.
- [11] N. Zhu, H. Chang, A. Franson, T. Liu, X. Zhang, E. Johnston-Halperin, M. Wu, H. X. Tang, *Appl. Phys. Lett.* **2017**, *110*, 252401.
- [12] P. Trempler, R. Dreyer, P. Geyer, C. Hauser, G. Woltersdorf, G. Schmidt, *Appl. Phys. Lett.* **2020**, *117*, 232401.
- [13] R. Schlitz, T. Helm, M. Lammel, K. Nielsch, A. Erbe, S. T. Goennenwein, *Appl. Phys. Lett.* **2019**, *114*, 252401.
- [14] Y. Khivintsev, G. Dudko, V. Sakharov, Y. Nikulin, Y. Filimonov, *Phys. Solid State* **2019**, *61*, 1614.
- [15] M. Vogel, P. Pirro, B. Hillebrands, G. Von Freymann, *Appl. Phys. Lett.* **2020**, *116*, 262404.
- [16] E. Albisetti, S. Tacchi, R. Silvani, G. Scaramuzzi, S. Finizio, S. Wintz, C. Rinaldi, M. Cantoni, J. Raabe, G. Carlotti, R. Bertacco, E. Riedo, D. Petti, *Adv. Mater.* **2020**, *32*, 1906439.
- [17] C. Chappert, H. Bernas, J. Ferré, V. Kottler, J.-P. Jamet, Y. Chen, E. Cambri, T. Devolder, F. Rousseaux, V. Mathet, H. Launois, *Science* **1998**, *280*, 1919.
- [18] S. Mendsich, V. Ahrens, M. Kiechle, A. Papp, M. Becherer, *J. Magn. Magn. Mater.* **2020**, *510*, 166626.
- [19] W. Ruane, S. White, J. Brangham, K. Meng, D. Pelekhov, F. Yang, P. Hammel, *AIP Adv.* **2018**, *8*, 056007.
- [20] A. Papp, G. Csaba, W. Porod, in *2016 IEEE Int. Conf. on Rebooting Computing (ICRC)*, IEEE, Piscataway, NJ **2016**, pp. 1–4.
- [21] C. S. Davies, A. Francis, A. V. Sadovnikov, S. V. Chertopalov, M. T. Bryan, S. V. Grishin, D. A. Allwood, Y. P. Sharaevskii, S. Nikitov, V. Kruglyak, *Phys. Rev. B* **2015**, *92*, 020408.
- [22] J. Chang, V. Sitzmann, X. Dun, W. Heidrich, G. Wetzstein, *Sci. Rep.* **2018**, *8*, 12324.
- [23] H. G. Bauer, P. Majchrak, T. Kachel, C. H. Back, G. Woltersdorf, *Nat. Commun.* **2015**, *6*, 8247.
- [24] J. Ziegler, <http://www.srim.org/> **2013**, [online] (visited on 05/05/2022).
- [25] Á. Papp, M. Kiechle, S. Mendsich, V. Ahrens, L. Sahin, L. Seitner, W. Porod, G. Csaba, M. Becherer, *Sci. Rep.* **2021**, *11*, 14239.
- [26] A. Prabhakar, D. D. Stancil, *Spin Waves: Theory and Applications*, Vol. 5, Springer, Berlin, Heidelberg **2009**.
- [27] N. Whitehead, S. Horsley, T. Philbin, V. Kruglyak, *Appl. Phys. Lett.* **2018**, *113*, 212404.



- [28] N. Whitehead, S. Horsley, T. Philbin, V. Kruglyak, *Phys. Rev. B* **2019**, 100, 094404.
- [29] R. Paschotta, *Encyclopedia of Laser Physics and Technology*, 1st edition, Wiley-VCH, New York **2008**.
- [30] P. Ambs, *Adv. Opt. Technol.* **2010**.
- [31] J. W. Goodman, Publishers, Englewood, CO **2005**.
- [32] R. A. Gallardo, P. Alvarado-Seguel, F. Brevis, A. Roldán-Molina, K. Lenz, J. Lindner, P. Landeros, *Nanomaterials* **2022**, 12, 2785.
- [33] W. J. Smith, *Modern Optical Engineering*, 4th Edition, McGraw-Hill Professional, New York **2007**.
- [34] S. Molesky, Z. Lin, A. Y. Piggott, W. Jin, J. Vucković, A. W. Rodriguez, *Nat. Photonics* **2018**, 12, 659.
- [35] M. Gołębiewski, P. Gruszecki, M. Krawczyk, *Adv. Electron. Mater.* **2022**, 8, 2200373.
- [36] J. C. Gartside, K. D. Stenning, A. Vanstone, H. H. Holder, D. M. Arroo, T. Dion, F. Caravelli, H. Kurebayashi, W. R. Branford, *Nat. Nanotechnol.* **2022**, 17, 460.
- [37] M. Kiechle, S. Mendisch, in *Magnonics Conference* **2019**.
- [38] J. Ding, T. Liu, H. Chang, M. Wu, *IEEE Magn. Lett.* **2020**, 11, 5502305.